# Final Report
# F49620-00-1-0320

# Adaptive Multiplexed Wavelength
# and Spatial Signal Processing

Duke University • December 01, 2005

Dr. David Brady

| # REPORT DOCUMENTATION PAGE | | *Form Approved*<br>*OMB No. 0704-0188* |
|---|---|---|

Public reporting burden for this collection of information is estimated to average 1 hour per response, including the time for reviewing instructions, searching existing data sources, gathering and maintaining the data needed, and completing and reviewing this collection of information. Send comments regarding this burden estimate or any other aspect of this collection of information, including suggestions for reducing this burden to Department of Defense, Washington Headquarters Services, Directorate for Information Operations and Reports (0704-0188), 1215 Jefferson Davis Highway, Suite 1204, Arlington, VA 22202-4302. Respondents should be aware that notwithstanding any other provision of law, no person shall be subject to any penalty for failing to comply with a collection of information if it does not display a currently valid OMB control number. **PLEASE DO NOT RETURN YOUR FORM TO THE ABOVE ADDRESS.**

| **1. REPORT DATE** *(DD-MM-YYYY)*<br>12/01/05 | **2. REPORT TYPE**<br>Final | | **3. DATES COVERED** *(7/1/2004 – 6/30/2005)*<br>5/15/00–5/15/05 |
|---|---|---|---|
| **4. TITLE AND SUBTITLE**<br><br>Adaptive Multiplexed Wavelength and Spatial Signal Processing | | **5a. CONTRACT NUMBER** | |
| | | **5b. GRANT NUMBER**<br>F49620-00-1-0320 | |
| | | **5c. PROGRAM ELEMENT NUMBER** | |
| **6. AUTHOR(S)**<br><br>David J. Brady, Mark A. Neifeld, Travis Blalock | | **5d. PROJECT NUMBER** | |
| | | **5e. TASK NUMBER** | |
| | | **5f. WORK UNIT NUMBER** | |
| **7. PERFORMING ORGANIZATION NAME(S) AND ADDRESS(ES)**<br><br>**AND ADDRESS(ES)** Department of Electrical and Computer<br>Engineering<br>University of Illinois<br>Urbana, IL 61801 | | **8. PERFORMING ORGANIZATION REPORT NUMBER**<br><br><br>UI Ref. No. A9355<br>Duke Ref.  Sub Award 02-181 | |
| **9. SPONSORING / MONITORING AGENCY NAME(S) AND ADDRESS(ES)**<br>AFOSR                    Major Daniel K. Johnstone, PhD<br>801 N. Randolph Street<br>SteSui732<br>Suite 732<br>Arlington, VA  22203-1977 | | **10. SPONSOR/MONITOR'S ACRONYM(S)**<br>AFOSR | |
| | | **11. SPONSOR/MONITOR'S REPORT NUMBER(S)**     AFRL-SR-AR-TR-06-0151 | |

**12. DISTRIBUTION / AVAILABILITY STATEMENT**

Approved for public release;  distribution unlimited.

**13. SUPPLEMENTARY NOTES**
The views, opinions and/or findings contained in this report are those of the author(s) and should not be construed as an official Department of the Air Force position, policy or decision, unless so designated by other documentation.

**14. ABSTRACT**
Adaptive Multiplexed Wavelength and Spatial Signal Processing was a Duke University collaboration with the Universities of Arizona and Virginia administered by the University of Illinois. The program leveraged multiplex sensor systems capable of abstracting target specific projections from the hyperspectral data cube without measuring unrelated data points designed at Duke with embedded real-time data abstraction on *Spectel* spectral information abstraction focal planes made at UVa and algorithms developed at Arizona. A photo-detector front-end-array chip was designed, fabricated and tested. This prototype chip has an array size of 2mm x 2mm, consisting  of 34 by 34 cells, with each cell of size 50um by 50 um. Each cell is an independently functioning photo detector. All the active and passive components, including photo diodes, preamplifiers, filters and other analog/digital peripheral circuits, are integrated on this single chip of standard TSMC 0.35um process with a 3.3V supply voltage.

**15. SUBJECT TERMS**
Spectral imaging, rotational shear interferometery

| **16. SECURITY CLASSIFICATION OF:** | | | **17. LIMITATION OF ABSTRACT** | **18. NUMBER OF PAGES** | **19a. NAME OF RESPONSIBLE PERSON**<br>**D. Brady** |
|---|---|---|---|---|---|
| **a. REPORT**<br>UNCLASSIFIED | **b. ABSTRACT**<br>UNCLASSIFIED | **c. THIS PAGE**<br>UNCLASSIFIED | UL | | **19b. TELEPHONE NUMBER**<br>*919-660-5394* |

Standard Form 298 (Rev. 8-98)
Prescribed by ANSI Std. Z39.18

# Table of Contents

**Summary**

Adaptive Multiplexed Wavelength and Spatial Signal Processing was a project under the DARPA Photonic Wavelength and Spatial Signal Processing Program. The project included spectral imaging system hardware development and testing at Duke University, system analysis and algorithm development efforts at the University of Arizona and spectral imaging focal plane development at the University of Virginia.

System development at Duke initially focused on rotational shear interferometer designs and included a variety of RSI system demonstrations. Subsequent studies led to revolutionary spectral sensor designs based on photonic crystals and coded aperture systems. The Duke team collaborated with the Arizona group in evaluation of spectral imaging system performance. The P-WASSP program at the University of Arizona has produced significant results in four areas: (1) nonlinear estimation for interferometric imaging, (2) information-theoretic analysis of imaging systems, (3) feature-specific imaging, and (4) super-resolution via nonlinear image combining. Jointly, the Duke and Arizona efforts produced 10 journal papers and 15 conference presentations.

The VLSI group at the University of Virginia designed an optical sensing front-end for interferometer imaging, The design goals for this stand-alone photo-detector chip on incoming modulated light, with modulating signal frequency around 15 KHz and carrier light wavelength around 650 nm.

## Publication List

- S. Basty, M. A. Neifeld, D. Brady, and S. Kraut, "Nonlinear Estimation for Interferometric Imaging," *Optics Communications*, Vol.228, pp.249-261, 2003.
- Amit Ashok and M. A. Neifeld, "Information-Based Analysis of Simple Incoherent Imaging Systems," *Optics Express*, Vol.11, pp.2153-2162, 2003.
- M. A. Neifeld and P. Shankar, "Feature-Specific Imaging," *Applied Optics*, Vol.42, pp.3379-3389, 2003.
- Himadri Pal and M. A. Neifeld, "Multi-Spectral Principal Component Imaging," *Optics Express*, Vol.11, pp.2118-2125, 2003.
- Himadri Pal, Dinesh Ganotra, and M. A. Neifeld, "Face Recognition by using Feature-Specific Imaging," *Applied Optics*, Vol.44, pp.3784-3794, 2005.
- P. Shankar, W. Hasenplaugh, R. Stack, R. Morrison, and M. A. Neifeld, "Multi-Aperture Imaging," submitted to *Applied Optics*, July 2005.
- Potuluri, P., M. R. Fetterman and D. J. Brady (2001). "High depth of field microscopic imaging using an interferometric camera." Optics Express 8(11): 624-630.
- Potuluri, P., M. E. Gehm, M. E. Sullivan and D. J. Brady (2004). "Measurement-efficient optical wavemeters." Optics Express 12: 6219-6229.
- Xu, Z. C., Z. L. Wang, M. E. Sullivan, D. J. Brady, S. H. Foulger and A. Adibi (2003). "Multimodal multiplex spectroscopy using photonic crystals." Optics Express 11(18): 2126-2133.

- K. Lepage, D. Thomson, S. Kraut and D. J. Brady, "Multitaper scan-free spectrum estimation using a rotational shear interferometer," to appear in Applied Optics, May 2006

## Spectral Imaging Systems

Initial studies under this program focused on the spectral imaging using rotational shear interferometers. Based on information theoretic and design analyses developed in collaboration with the Arizona group, the project expanded to include photonic crystal and coded aperture imagers. Coded aperture hyperspectral imaging resolves the "missing cone" problem encountered throughout the P-WASSP program. Continuing work in this regard is described in Gehm, M. E. and D. J. Brady (2006). High-throughput hyperspectral microscopy. Three-Dimensional and Multidimensional Microscopy: Image Acquisition and Processing XIII, San Jose, CA, USA, SPIE.

For background on the original thrust of this program, this document describes spectral imaging on the rotational shear interferometer.

### The Rotational Shear Interferometer

The RSI is similar to a Michelson interferometer except that the planar mirrors on the arms are replaced by right-angle folding mirrors. Fig. 1 shows a diagram of an RSI.
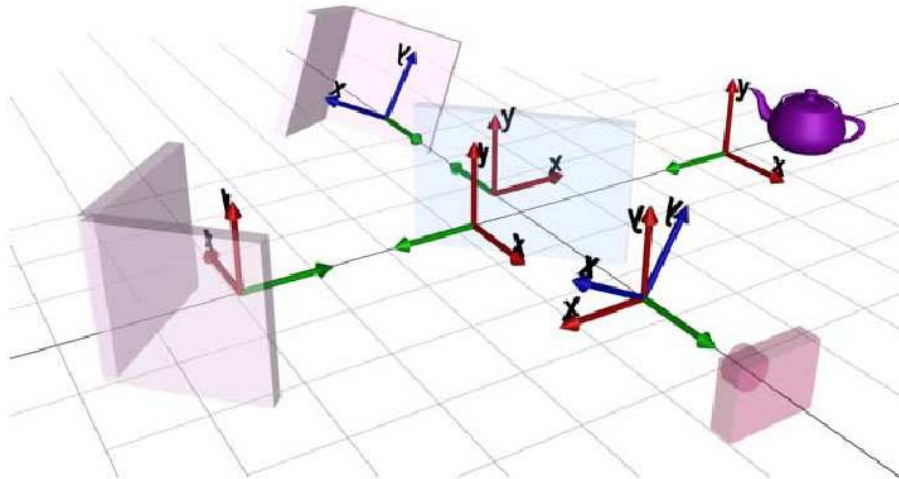


Fig 1. Diagram of a rotational shear interferometer

The RSI allows us to measure the mutual coherence of the incident wavefront by interfering the wavefront with a rotated and time-delayed version of itself. One of the arms of the RSI can be rotated about the optical path, producing the shearing angle. A wavefront incident upon the RSI is initially split by the beam splitter and then traverses both of the arms. One of the arms folds the wavefront while the other both folds and rotates the wavefront. The arm with the rotation mechanism is also translatable, allowing for a path length difference between the two arms, just like a Michelson interferometer.

After traversing the arms, the wavefront is recombined and imaged on a digital focal plane.

The RSI has been used in astronomy, primarily during the 1970s and 1980s before adaptive optics became available to the astronomy community. All uses of the RSI during this period applied the van Cittert-Zernike theorem [1]. This theorem states that under the restriction of a quasi-monochromatic spectrum, a measurement of mutual intensity from a source is equivalent to the Fourier transform of the spatial intensity distribution of the source. This allows astronomers to reconstruct the image of a star from the FFT of the interference pattern recorded with an RSI from a telescope and narrow band spectral filter. Initially, Breckenridge analyzed an interferometer identical to an RSI with the shear fixed at 90 degrees [2]. His goal was to take high resolution astronomical images through the atmosphere. He collected a set of short exposure interference patterns, eliminated the interference patterns that were distorted by atmospheric turbulence, and combined the remainder for analysis. Later, the RSI was used and analyzed by Roddier, Mariotti, and Chelli for successful stellar observations [3-8]. In all cases, photon efficiency was a serious problem because of the narrow band spectral filters used to meet the quasi-monochromatic source condition.

### Spatio-Spectral Triangulation

If we consider a monochromatic point source with wavelength $\lambda$ and at distance $r$, the field due to this source is a spherical wave, E(r).

$$E(r) = \frac{A}{r} e^{i2\pi\frac{r}{\lambda}}$$

When we measure this field with an RSI, the CCD measures the sum of fields reflected from the two arms of the interferometer. If we neglect the amplitude factor, and let $r_1$ and $r_2$ be the distances of the point source through two arms of the interferometer, we arrive at the following expression for the field at the CCD.

$$E_{CCD} \propto e^{i2\pi\frac{r_1}{\lambda}} + e^{i2\pi\frac{r_2}{\lambda}}$$

The CCD measures the intensity, or square of the magnitude, of this electric field. Simple trigonometry identities convert this expression to the sum of a constant and a cosinusoidal term.

$$I_{CCD} \propto \left| e^{i2\pi\frac{r_1}{\lambda}} + e^{i2\pi\frac{r_2}{\lambda}} \right|^2 = 2 + 2\cos\left(\frac{2\pi}{\lambda}(r_1 - r_2)\right)$$

For a monochromatic point source, the RSI produces a two dimensional sinusoidal fringe pattern that can be analyzed with an FFT. A simulation of the RSI's response to a monochromatic point source is shown in Fig. 2.
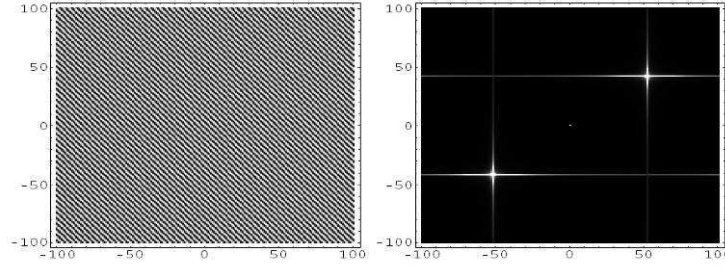
Fig. 2. RSI response to a monochromatic point source and the FFT of this fringe pattern

The spatial and spectral information in this fringe pattern are linked such that you cannot solve for the absolute angular position and wavelength unless two measurements are made from different positions.  Each measurement provides an estimate of the target's position.  The angular position of the point source occurs at the intersection of the two estimates.  The two measurements can be made with a single RSI that is slightly rotated between measurements or by a pair of RSI's that have a known misalignment between their optical axes.  The following equations can be used determine the position ($\phi_x$) and wavelength ($\lambda$) of the point source:

$$\tan\left(\phi_x\right) = \frac{1}{2\tan(\Delta\phi_x)v_2}\left(v_2 - v_1 - \sqrt{\left(v_1 - v_2\right)^2 - 4v_1 v_2 \tan^2(\Delta\phi_x)}\right)$$

$$\lambda = \frac{\sin(2\theta)}{\tan(\Delta\phi_x)v_1 v_2}\left(v_2 - v_1 - \sqrt{\left(v_1 - v_2\right)^2 - 4v_1 v_2 \tan^2\left(\Delta\phi_x\right)}\right)$$

In these equations, $\theta$ is the shear angle of the RSI, $v_1$ and $v_2$ are the horizontal components of the spatial frequency of the sinusoid for the first and second measurements, and $\Delta\phi_x$ is the misalignment between the two measurements.

For a non-monochromatic point source, a similar analysis works to resolve the target's position – the intensity of the two dimensional sinusoid is modulated by a function containing the spectral data.  Again, the FFT or a two dimensional sinusoid fit algorithm can be used to determine the parameters required to solve for angular position.  In this case, however, the FFT of the fringes shows spectrum of the point source convolved with reconstructed points.  An example of this is shown in Fig. 3, based on an RSI's response to a white LED in the lab.
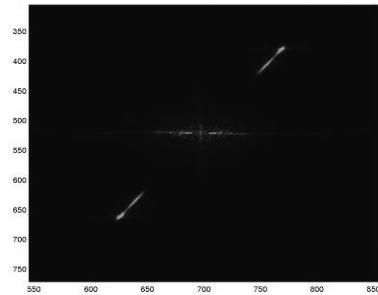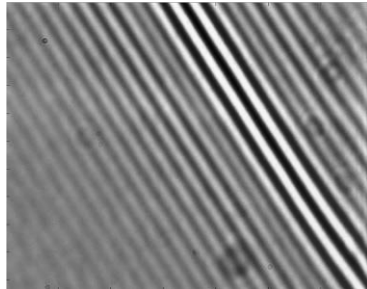
Fig. 3. RSI fringes from a white LED and their FFT

In Fig. 3 two copies of the spectrum of the point source appear along the radial line between the two stretched points in the image. The second measurement of the source provides a factor to determine the proper scaling of a spectrum taken along the radial line. The spectrum taken from Fig 3 is shown beside a spectrum measured with an Ocean Optics spectrometer in Fig. 4.
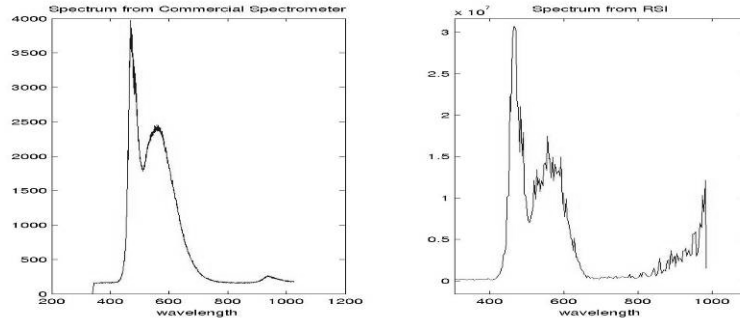


Fig. 4. White LED spectrum measured by RSI and a commercial spectrometer.

The response for the RSI above 800nm is due to the low frequency noise that can be seen in the center of the FFT picture in Fig. 3.


**Analysis and Estimation**

INonlinear Estimation for Interferometric Imaging

In this work we have conducted a comparative study of two different imaging systems for distant point sources. One is a conventional focal plane system and the other is a non-traditional system based on a rotational shearing interferometer (RSI). The RSI produces a linear fringe pattern in response to each object point source. Within the P-WASSP program we have developed a new nonlinear algorithm for estimating point source parameters in an RSI and we have found that this new nonlinear method outperforms traditional Fourier methods. In order to compare the RSI with a conventional focal plane system we have characterized the intensity- and position-estimating ability of these two optical systems in the presence of noise. In order to make our comparison fair, we developed a nonlinear algorithm for use with conventional systems and compare its performance with that of our nonlinear RSI post-processing method. We find that the RSI is always inferior to the conventional imager for additive white Gaussian noise dominated measurements; however, the two imaging systems provide comparable performance in the shot-noise limit.

We have also studied the super-resolution ability of our nonlinear estimation algorithm for pairs of nearby monochromatic point sources. Figure (5) shows how our nonlinear algorithms can provide position estimates (RMSE) of approximately 0.01 pixels based on

either conventional or RSI imagers; whereas, linear methods (e.g., FFT-based) provide no better than RMSE=0.2. We have also extended our nonlinear estimation algorithm to the domain of multi-spectral RSI imaging. Given a single polychromatic point source characterized by M wavelength bands we find an optimal estimate of position and intensity. Once again we find that the performance achieved using an RSI is comparable to that achieved using a conventional imager.

Information-Theoretic Analysis of Simple Incoherent Imaging

In this work we have studied the information capacity of a few simple incoherent imaging systems. Previous efforts along this direction have generally assumed a Gaussian model for the object space; however, in most instances this model is not adequate. We have taken a different approach in which we assume that the object space comprises relatively few equal intensity point sources. In this case it is possible to completely describe the object configuration using a list of point-source-positions and the role of the imager is therefore to provide measurements that facilitate the optimal estimates of these positions. Toward this goal we define the information capacity of an imaging system as the mutual information between the object space and the measurement space. Using this metric we have analyzed three candidate imaging systems: (1) a conventional lens imager, (2) a cubic phase mask imager, and (3) a random phase mask imager. We find that the use of a random phase mask can maximize the measurement entropy and in low-noise conditions can be used to maximize the imaging mutual information (IMI). For example, we find the rather surprising results that with only a single detector element, images of a single point source using a random the IMI achieved by a conventional lens imager. Two such random phase mask imagers deployed at 90 degrees to the object space can provide IMI=89% of the total scene information. We find that the cubic phase mask provides performance between these two extremes, exchanging axial information for lateral information as shown in Figure (6).

Feature-Specific Imaging

This work represents the most significant element of our P-WASSP program. In this activity we have studied incoherent optical systems that can directly measure linear projections of the optical irradiance distribution. We find that such direct feature measurement exploits the multiplex advantage and for small numbers of projections, can provide higher feature-fidelity than those systems that post-process a conventional image. We have verified this observation using a large number/variety of features including various types of wavelets, principal components (PC), Hadamard features, independent components, and Fisher features. It should also be noted that the direct measurement of (relatively few) linear projections also results in significant dimensionality reduction. Feature-specific imaging can therefore be used to reduce the complexity of imager hardware and/or increase the frame rate of image acquisition.

We have studied several applications within which high-fidelity feature measurements can be used. The first application exploits high-fidelity PC feature measurements in an effort to reconstruct a high-fidelity estimate of the original object. In this case we find an

interesting/important tradeoff: increasing the number of measured PC features reduces the truncation error associated with the object reconstruction; however, it also increase the number of required measurements and thus increases the measurement noise. There is an optimal number of features as shown in figure 7 for a noise variance of 500. Plotting these optima as a function of noise level results in the plot of figure 8. It is important to see that feature-specific imaging is superior for noise levels beyond    =8. The extension from monochromatic feature-specific imaging to multi-spectral feature-specific imaging is straightforward and results in even more significant performance improvements as shown in figure 9. These results are obtained from seven-band LANDSAT-7 data and some example images are shown in figure 10a (conventional measurement) and 10b (feature-specific measurement).

We have also studied feature-specific imaging for use within an automated pattern recognition environment. Wavelet, PC, and Fisher features were investigated for a face recognition application. Once again it was our intent to exploit the high feature-fidelity afforded by features-specific imaging in order to realize significant gains in recognition performance. Figure 11 is an example comparison between conventional imaging and feature-specific imaging using a neural recognition algorithm. We see that an extraordinary degree of noise tolerance is provided by use of the feature-specific approach.

Nonlinear Image Combining

In this work we seek to combine several low-resolution measured images in order to obtain a high-resolution estimate of the object. This is common practice in cases for which the image resolution is limited primarily by the pixel-size of the camera. In these cases the camera can be dithered on a sub-pixel scale in order to provide "shift diversity" and allow recovery of details below the pixel size limit. In our activities we have pursued the use of (a) multiple cameras as opposed to a single dithered camera and (b) the use of additional dimensions of diversity (e.g., shift, rotation, scale, and fill-factor) in order to provide a better-conditioned inversion to the resulting image reconstruction problem. We have adapted the conventional iterative back propagation (IBP) method to the new inversion problem represented by (a) and (b). The performance of our new algorithm can be seen from the example in figure 12 in which the camera SNR=46dB and the measured low-resolution images are 4x under-sampled in both dimensions. In this example we plot the RMSE of the reconstructed object as a function of the number of imagers used in the reconstruction. The curve representing high-diversity is seen to outperform the other two cases. Figure 13 depicts some example reconstructions and we see that excellent visual quality is achieved by use of 32 low-resolution cameras.
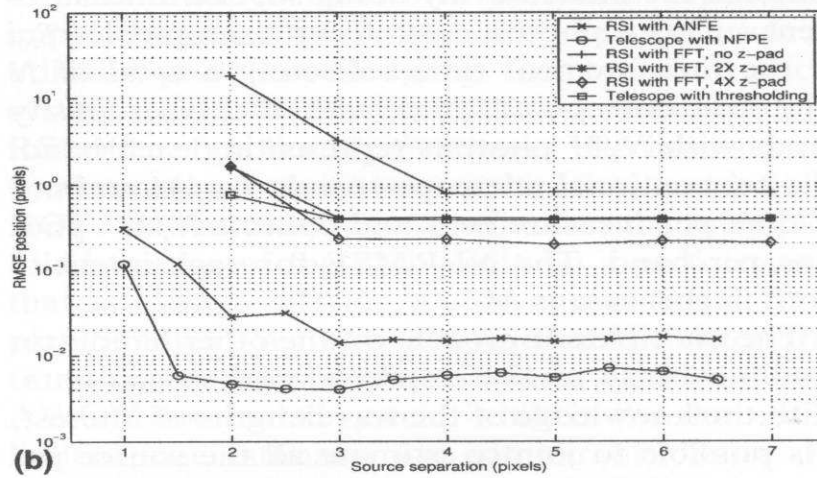
**Figure 5: RMSE position estimation versus actual source separation for two equal-intensity monochromatic point sources**
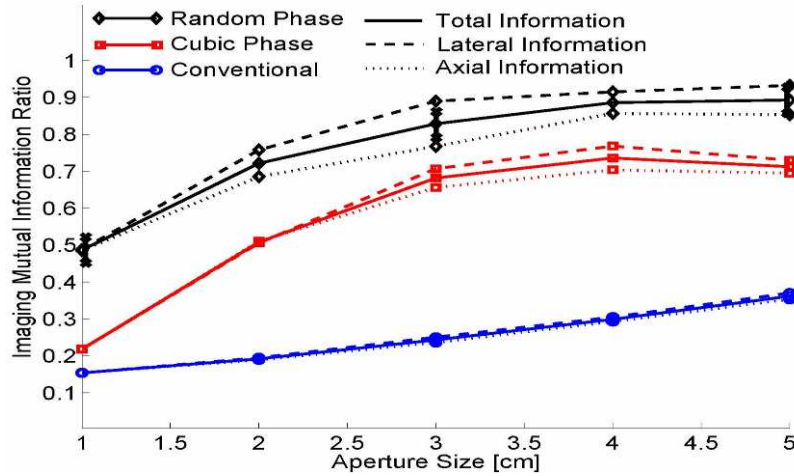


**Figure 6: Information capacity of a two-aperture imager (90 degree configuration) in which each aperture employs a single detector pixel.**
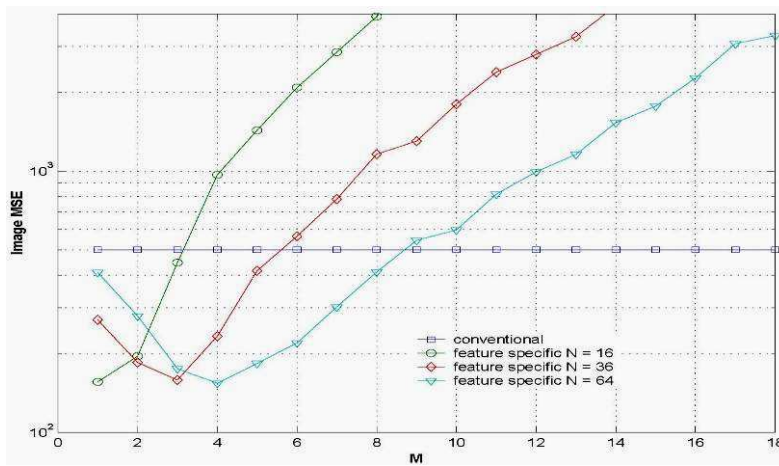
**Figure 7: Reconstruction MSE versus number of measured features for PC feature-specific imaging with AWGN $\sigma^2=500.$**
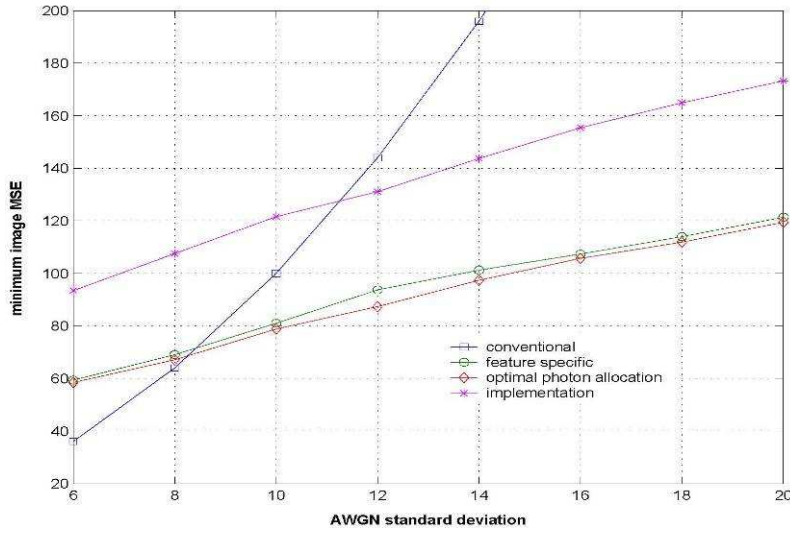


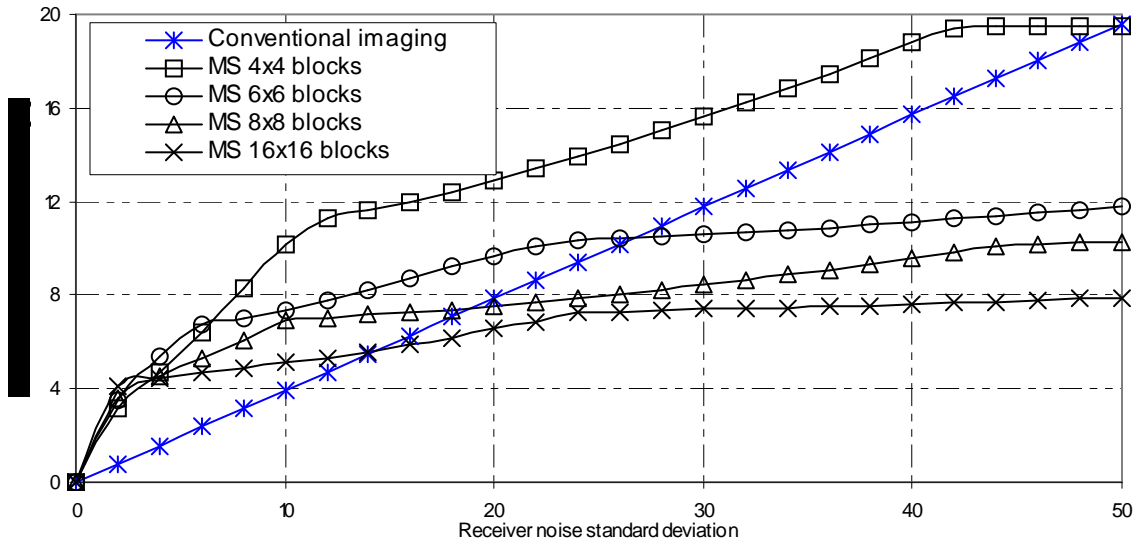**Figure 8: Optimal PC feature-specific imaging performance versus noise strength**.



**Figure 9: Minimum reconstruction RMSE versus noise strength for seven-band LANDSAT-7 images.**
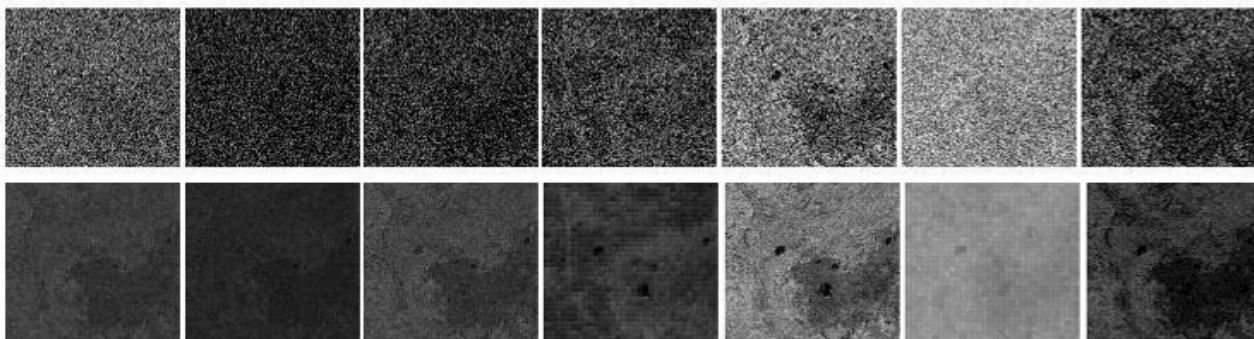
**Figure 10: Example reconstructions from LANDSAT-7 images at noise s=40. Top row is for conventional imaging and bottom row is for feature-specific imaging with 16x16 blocks.**
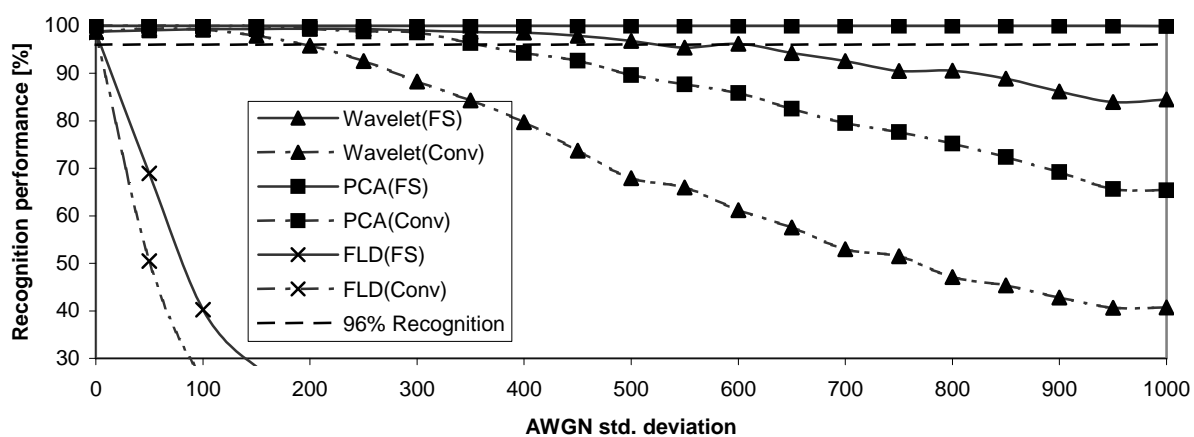


**Figure 11: Recognition performance versus noise strength for conventional (dashed) and feature-specific (solid) imaging using three different types of feature and a neural net.**
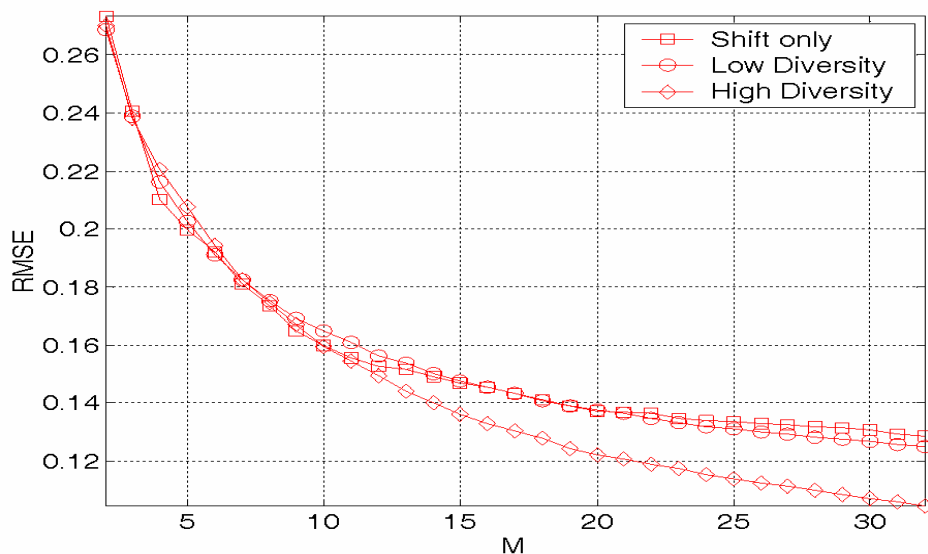
Figure 12: Reconstruction RMSE versus the number of low-resolution images for the case of 4x under-sampling and SNR=46dB.



(a)          (b)          (c)          (d)

Figure 13: Reconstructed images at SNR=54dB with 4x under-sampling and using (a) M=2, (b) M=4, (c) M=8, and (d) M=32

Design and testing a photo-detection chip

1). Realizing all functionalities and components on a single chip is a fundamental advantage as well as a challenge of using
     VLSI  technologies.
2). Firstly, convert incoming light to current and, at the same time, demodulate the signal from carrier into signal frequency
     range.
3). Secondly, convert current to voltage, and
4). Amplify ac voltage to ease the requirements on front-end signal processing
5). Then, perform front-end signal processing by getting rid of the dc information, and extracting ac voltage to get amplitude
     and phase information.
 --- 2), 3), 4) and 5) are the functionalities of each individual pixel, which has same structure but functions independently.
6). Replicate the pixel in a 2-dimension space to form an array, so that relative amplitude and phase among each pixel in the
    array can be extracted and then processed by digital signal processing (DSP processing is the topic of another research
     group)
7). Hard limits for the pixel and array design are pushed to achieve:  high fill factor ( > 10% ), small area (to allow at least
     32x32 pixels on a single chip for DSP processing),  adaptive input dc level(large input light dynamic range).
8). Soft limits such as low noise level, power and speed, as a trade-off, are relaxed only if the hard limits could not be
     achieved under other constraints.
9). Add only necessary peripheral circuitry to facilitate array operation and data/control I/O.
10). Design appropriate testing bench for chip testing.

At the chip level, as shown in Fig. 14, the array is operated by control logic with control I/O and data I/O.
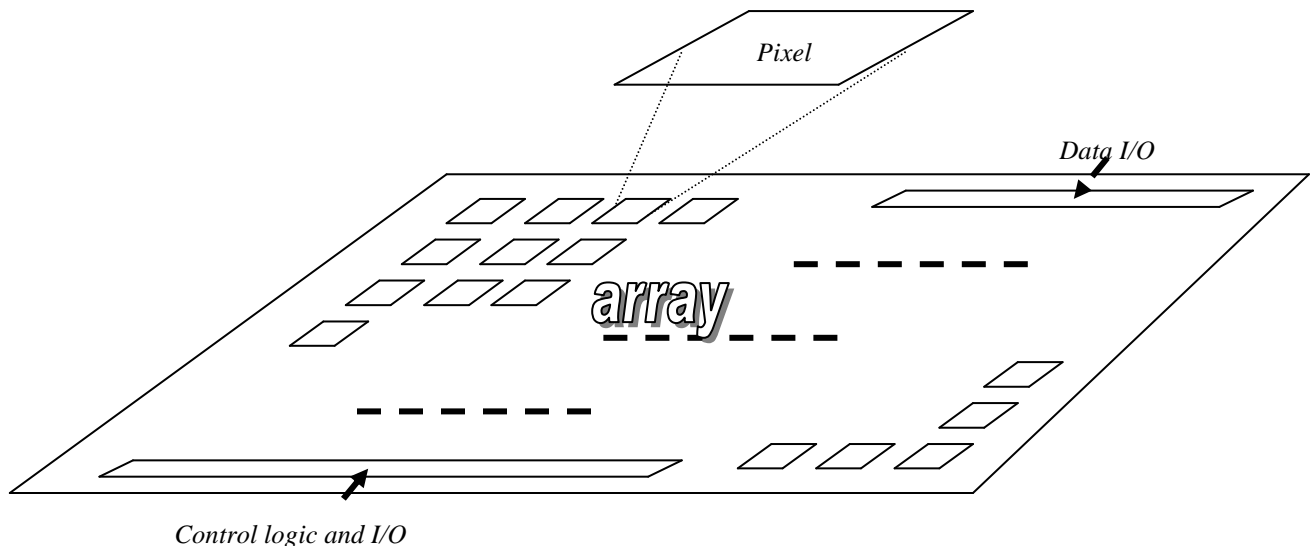


*Control logic and I/O*

Figure 14. Chip block diagram

At the pixel level within the array, as shown in Fig. 15, the design comprises an optical signal converting unit (hereafter also called part 1) and a signal extracting unit (hereafter also called part 2) to fulfill the design goals of 2), 3), 4) and 5).
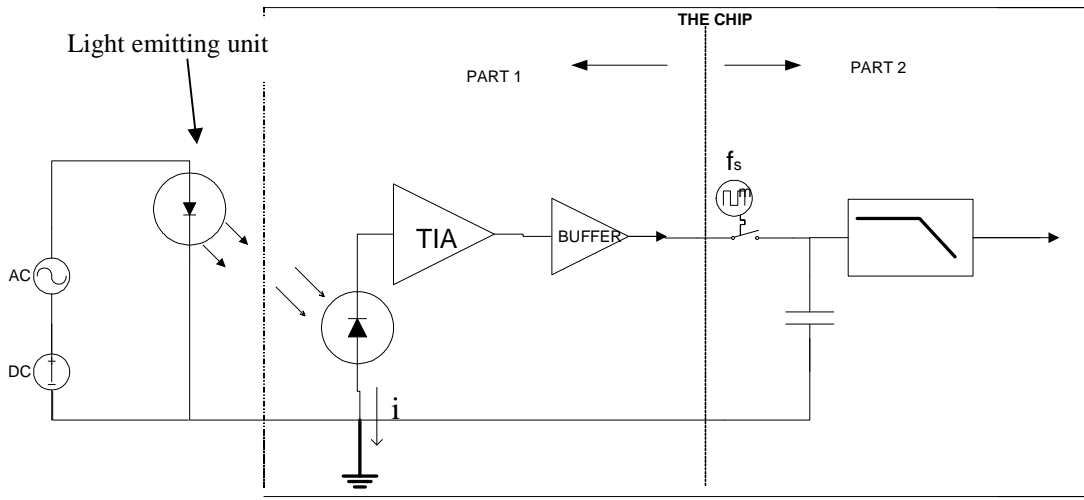


Figure 15. The sketch of the pixel, including part1 and part2 (except that those outside the box, i.e. the AC, DC sources, and photo-emitter on the left side of the sketch, are not in this design. But they are included for illustration purpose)

## II. Optical Converting Unit Design And Analysis

A. Photodiode

The optical converting unit (part 1) first converts the optical signal into a signal current via silicon photodiodes implemented by standard on-chip N-well/P-substrate structures. This photodiodes also perform demodulations[12]. The reverse-biased photodiode allows a continuous current, including background current, signal current and other noise current, to flow as long as the diode is situated in a circuit loop.
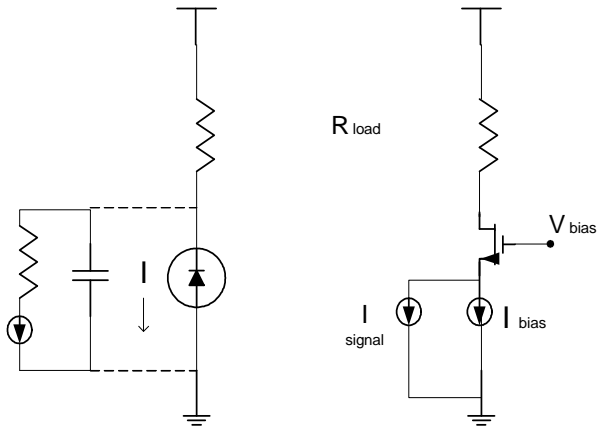
Figure 16. The photodiode and the I→V converting via resistor/transistor.

Left: A photo diode and a resistor form a simple I→V conversion. (The R, C and a current source on the left of photodiode, connected by dash lines, form a circuit model for the photodiode)

Right: Additional biasing and a transistor are added into the simple photodiode + resistor structure for a better I→V conversion.

On the left side of Fig. 16, a simplified model for this photodiode is shown on the left of diode[12]. This on-chip photodiode significantly eliminates parasitic effect of off-chip commercial photodiode. For good precision in signal sensing and processing, low element area and high fill factor are required.

B. TIA

A transimpedance amplifier (TIA) then converts photocurrents detected by the photodiode into voltages. The TIA is commonly dc coupled with the photodiode, as shown on the right side of Fig. 16. A common gate stage is used here to convert current to voltage with the dc bias point set by a dc current source, labeled as $I_{bias}$. Transimpedance gain is determined by a load resistor. In the practical on-chip realization, this load resistor is implemented by an active PMOS transistor ( called "$P_{load}$" in Fig 17). A simplified TIA schematic is shown in Fig. 17.
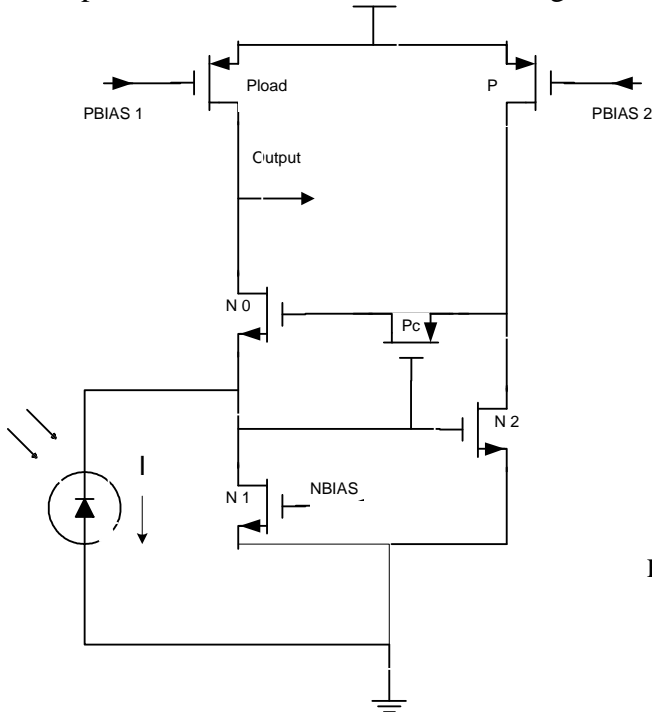


Figure 17. Transimpedance amplifier schematic  (TIA)

The overall final TIA structure has an extra MOSFET and its biasing path on the right side to reduce the input impedance of the common gate, so that almost all the signal current will be sucked into load resistor. The input impedance is reduced to be 1/A after this extra transistor added, where A is the loop gain for the loop around this extra MOSFET amplifier. Another benefit of this extra circuitry is a much more stable reverse bias for the photodiode, and thus reduces associated noises due to photodiode biasing fluctuation.

The transfer function of this unit is :       $V(out) \, / \, V^{||}(in) \, = \, R_{load} \; = \, r_{\,n\text{-}o} \quad r_{\,p\text{-}load}$
(1)

TIA's small signal model is shown in Fig. 18. From simulation, Fig. 20 shows transimpedance is around 150 db from DC up to 1 MHz. A more accurate model will be a second–order transfer function calculated from small signal model with additions of input capacitor C1and load capacitor C2:

$$\frac{Vout}{Iin} \; = \; \frac{(g_m + g_{mb})\, R_{load}}{(g_m + g_{mb} + C_1 s)\,(R_{load}\, C_2 s + 1)} \tag{2}$$

The noise model of this common-gate stage is shown in Fig. 19. Refered back to the input node, the input-referred equivalent thermal noise current is 570 $fA \, / \, Hz^{\,1/2}$ for $g_{m\text{-}n1} = 20.9$ $uS$ and $g_{m\text{-}pload} = 9.4 \; uS$, while the total thermal noise over a band of 50 $kHz$ is $1.63 \times 10^{-20} \, A^2$. The flick noise referred back to input is calculated as a total of $7.053 \times 10^{-20} \, A^2$ for a band of 50 $kHz$. This leads to total calculated noise of $8.68 \times 10^{-20} \, A^2$ for our choices of transistor sizes. TIA input equivalent noise is simulated to be about 800 $fA \, / \, Hz^{\,1/2}$ up to 100 $MHz$ and output equivalent noise is about 6.3 $uV \, / \, Hz^{1/2}$ in the middle band. Equations for noise calculations are listed below.  (Equation 3 is for thermal noise, equation 4 is for flicker noise, and equation 5 is for total noise).

$$\overline{I^{\,2}_{n,in-t}} \; = \; 4\, kT \quad \tfrac{2}{3} (\, g_{m-n1} \; + \; g_{m-pload} \;) \tag{3}$$

$$\overline{I^{\,2}_{n,in-f}} \; = \; \frac{1/f}{C_{ox}} \left[ \frac{g^{\,2}_{m-n1}\, K_{n1}}{(WL)_{n1}} \; + \; \frac{g^{\,2}_{m-po}\, K_{po}}{(WL)_{po}} \right] \tag{4}$$

$$\overline{I^{\,2}_{n,in-total}} \; = \; \int_{1}^{50k} (\, \overline{I^{\,2}_{n,in-t}} \; + \; \overline{I^{\,2}_{n,in-f}} \,) \; df \tag{5}$$

Figure 18. Small signal model of TIA
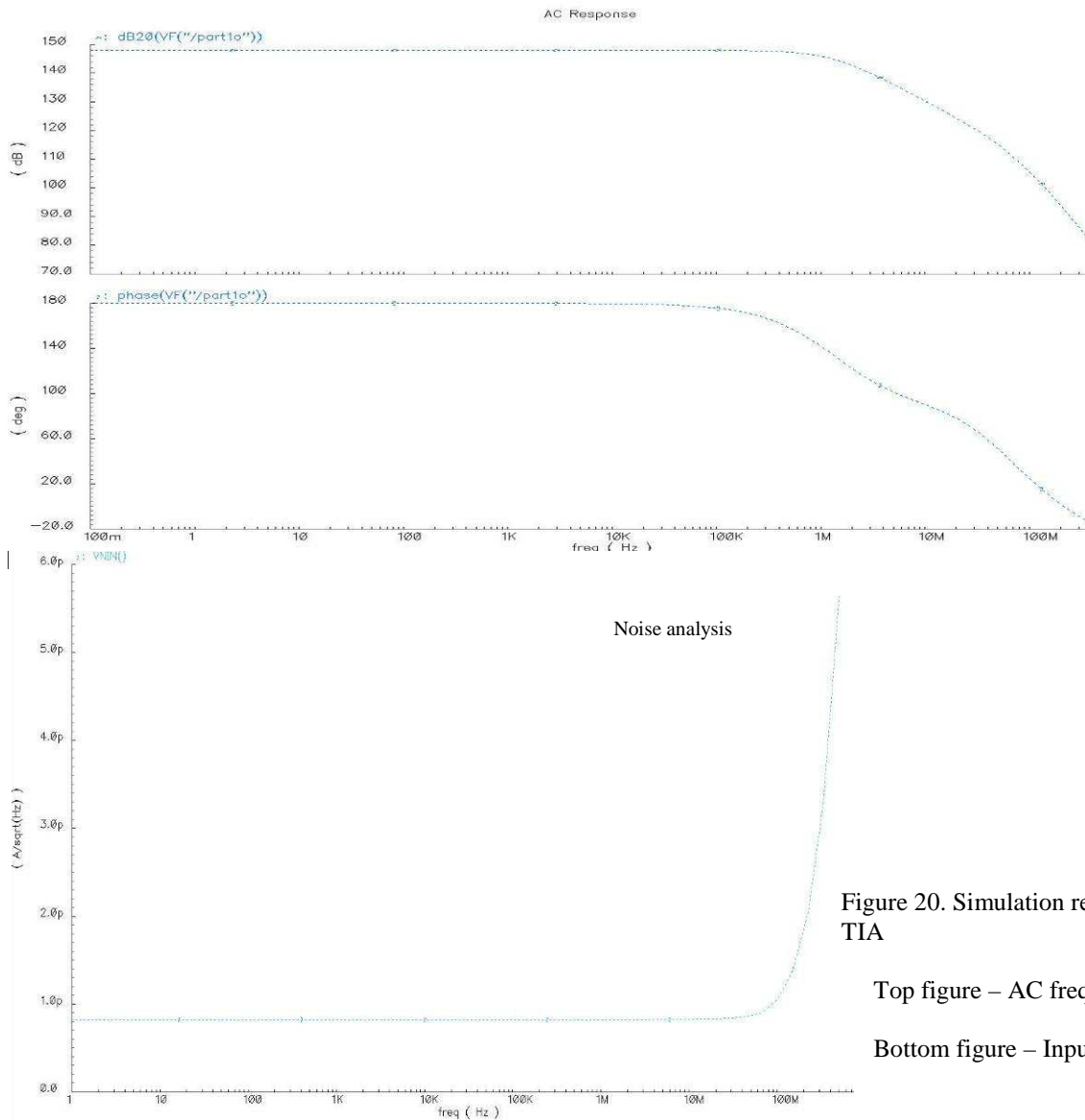


Figure 19. Noise model for TIA

Figure. 20
(top figure)

Figure 20. Simulation results (AC and Noise) of TIA

Top figure – AC frequency response

Bottom figure – Input equivalent current noise

The signal obtained from the optical converting unit is represented by three parameters, frequency, amplitude and phase. Because we already know its frequency, we can reduce the whole waveform to only three points of this signal by using a signal extracting unit (ie. a frequency selective filter, including a frequency selective sampling switch and a holding capacitor), followed by low-pass filters to filter out high frequency components and noises [11]. These three points together will give magnitude and phase information, and therefore the original sinusoid signal. This filter works better than other continuous time filters for signals with known frequencies and being digitized, but noise is one of the major sources of error in outputs of this filter.

A . Frequency selective

The above concept is transformed to a simple diagram shown in Fig.21. A switch samples an input sinusoid signal and deposits sampled charge on a holding capacitor. When the sampling frequency coincides with the signal frequency, the voltage held on the capacitor gets rewritten every time the switch samples. Thus a constant voltage results. Depending on the phase difference between input sinusoid and sampling pulse, this sampled constant voltage can be at any point of input sinusoid waveform. The top part of Fig. 9 from simulation shows this concept.
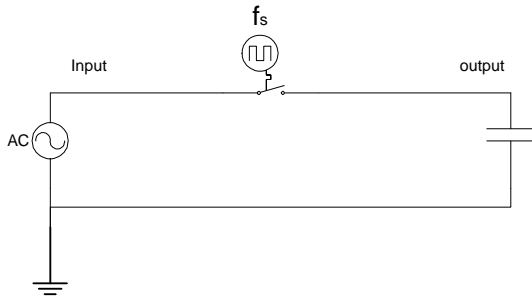


Figure 21. Simplified model of frequency selective filtering

On the other hand, if two frequencies are not the same, the voltage on the hold capacitor will step up and down on different sampling moments with an overall averaging effect (after low-pass filters) to be the dc voltage of the input sinusoid signal. This voltage is always the same no matter the phase difference between input sinusoid and sampling pulse. The bottom part of Fig. 22 shows this concept. Thus we can frequency selectively sample input signals. The block diagram of the filter implemented in CMOS is shown in Fig.23.

B. Low pass filter

To extract dc constant voltage from holding capacitor, a low pass filter with dynamic gate biasing technique is needed for filtering with very low corner frequencies. As the size of the on-chip capacitor is limited, a very large active resistor is needed to achieve a very low corner frequency. But this resistor can not be too large as it determines the time constant of the filter so that the output can reach its final value fast enough. This trade-off requires a dynamic gate biasing technique on the active MOSFET resistor. The dynamic gate biasing circuit samples the output voltage and adjusts accordingly the gate voltage of active MOSFET resistor by using source followers.

C. Noise analyses

Major noise sources associated with the sampling switch can be approximated by a RC structure, which has an equivalent noise voltage on the capacitor as approximately ( $kT/C$ )$^{1/2}$ for infinite bandwidth. So with a 1-pF capacitor, the total noise voltage at output is equal to 64.3 $uV$. There are also noises from channel charge injection and clock

feedthrough, among others from the switch structure. These effects result in three types of errors in MOS sampling circuits: gain error, dc offsets, and nonlinearity.

For an active RC low-pass filter, its thermal noise voltage is $(\ kT/C\ )^{1/2}$ , too. Flicker noise (1/f noise), which is significant at low frequencies, also plays an important role in the total noise power. In addition, small ripples around the low-pass filter corner frequency goes through the filter and results in uncertainty in measurement of final dc output. Finally, different time constants due to different input voltage levels will affect the speed of filter to achieve the final dc level. Thus samples measured at begining may have larger deviations from the correct dc value. These last two effects happen to conflict, improving one will deteriorate the other, especially when simulation models are inaccurate for transistors working under subthreshold or turn-off region. The output equivalent noise from simulation is shown in Fig.24.
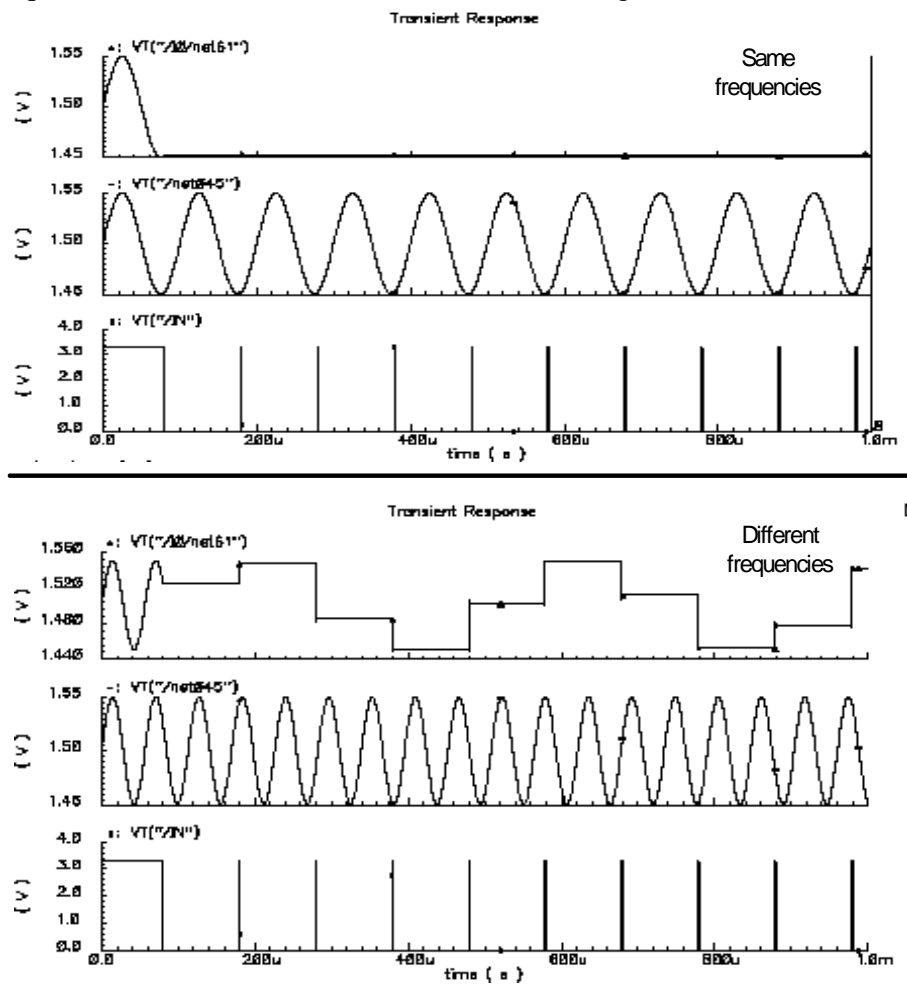


Figure 22. Sampling effects of frequency selective filtering. ( In both "same frequencies" and "different frequencies", the individual waveform are, from top to bottom, clock signal, input sinusoid, output voltage at holding capacitor )
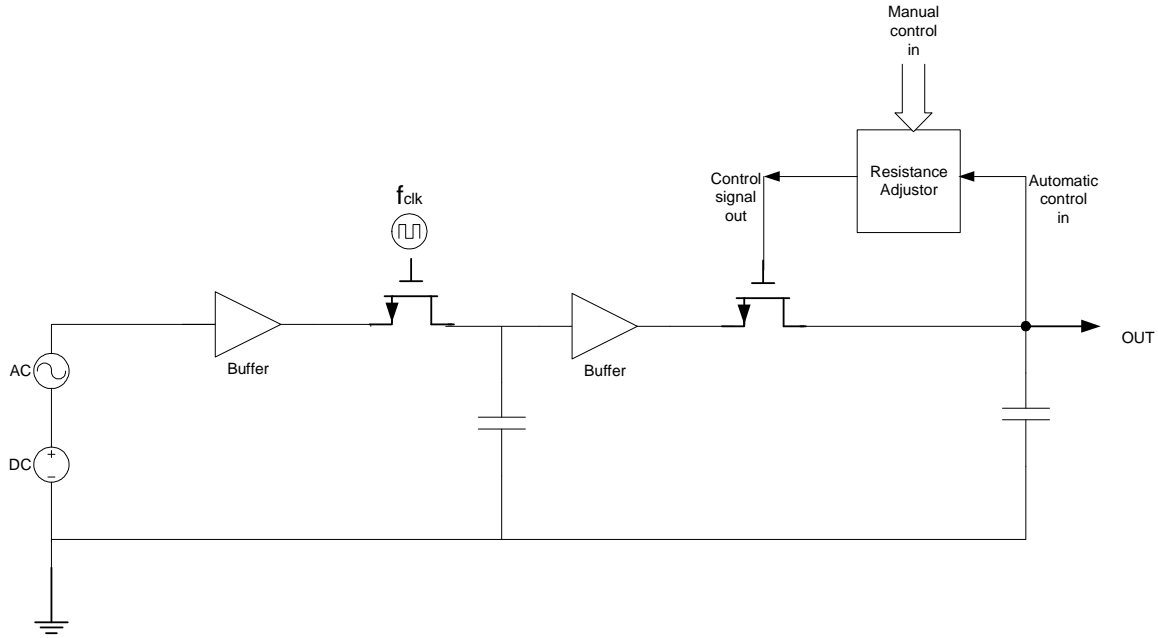
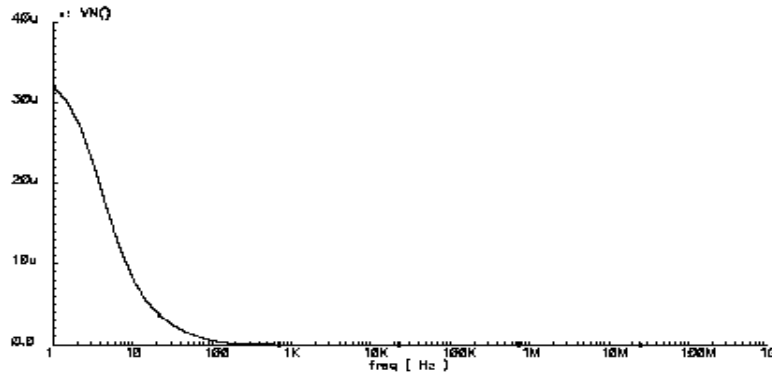Figure 23. Schematic of frequency selective filter



Figure 24. Output equivalent noise of frequency selective filter

The design was implemented in TSMC (Taiwan Semiconductor Manufacture Corporation) 0.35um analog & mixed-signal silicon VLSI process due to its availability and moderate low cost, compared with other processes from MOSIS. Latest fabrication was in April, 2004, with testing has continued since then. This section describes the results of on-chip implementation and testing. Fig 12. and 13 shows the top level schematic and layout, respectively. Fig. 27 shows those control bus and data line connections between pixels inside the array. The fabricated chip is shown in Fig. 28 with testing bench shown in Fig. 29.
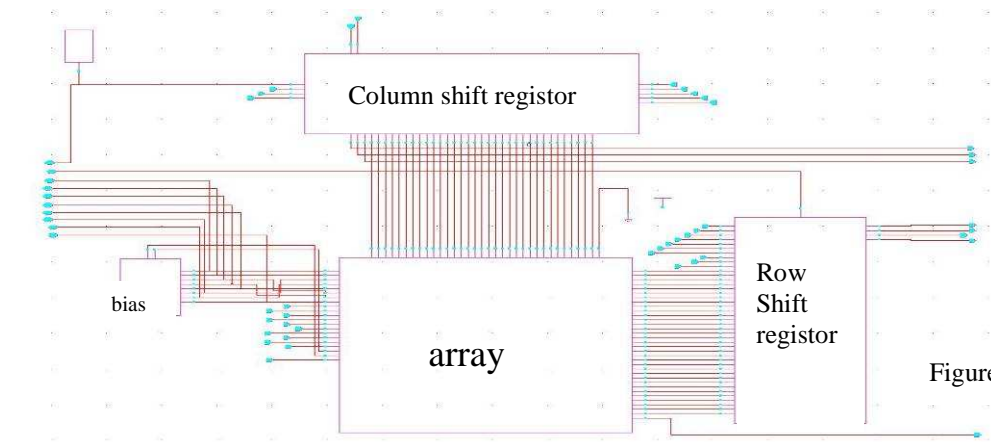
Figure 25. Top level chip schematic

Column shift register

Bias

Row shift register
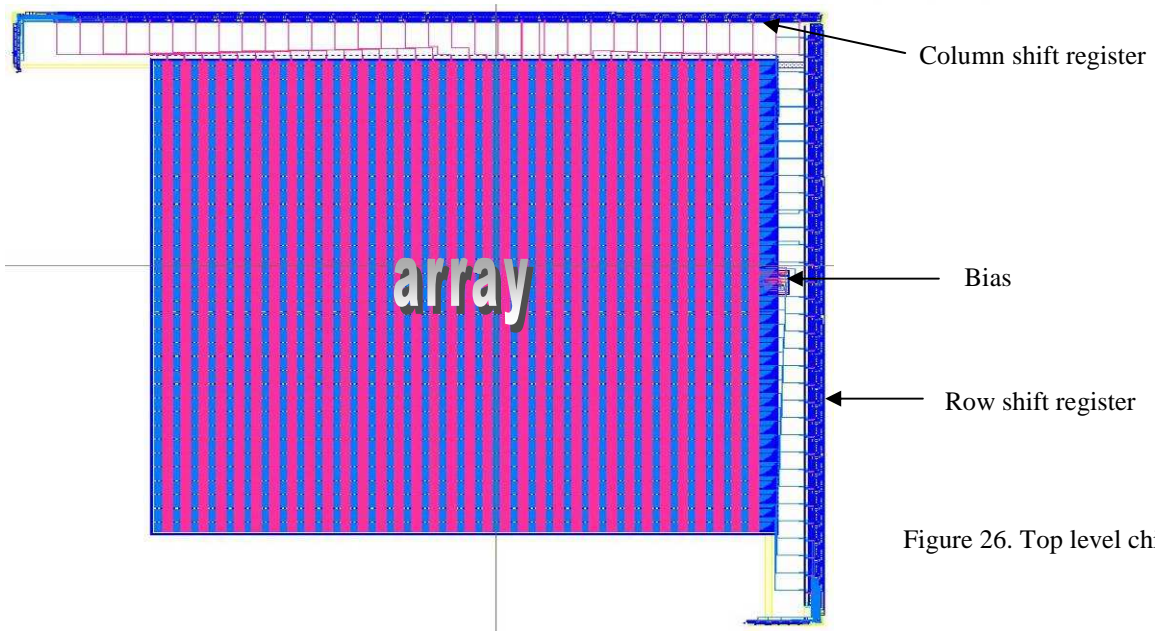
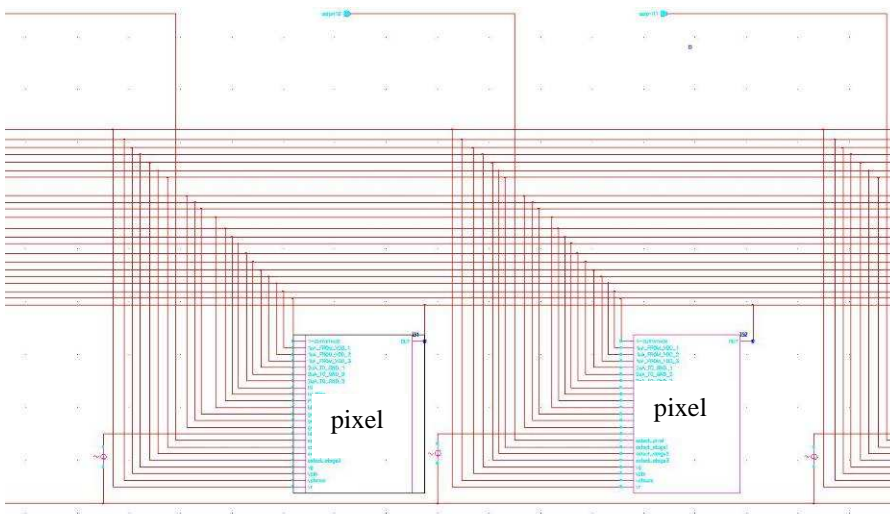Figure 26. Top level chip layout

pixel pixel
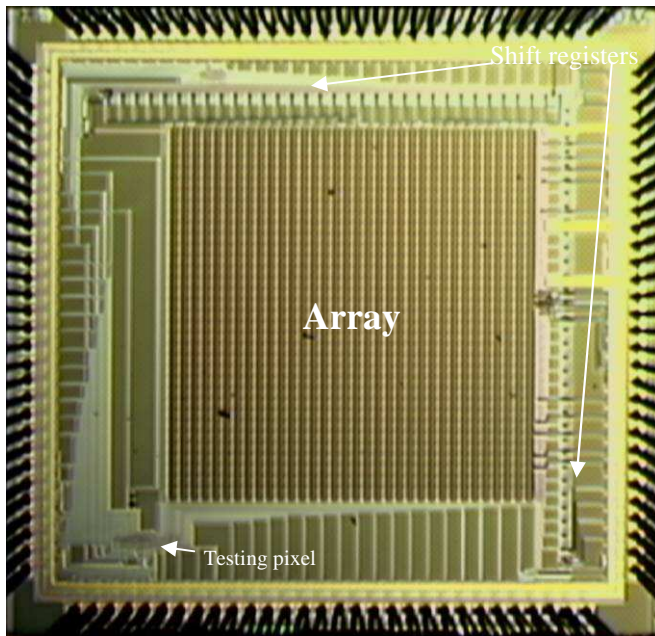
Figure 27. Pixels inside array
(schematic view)

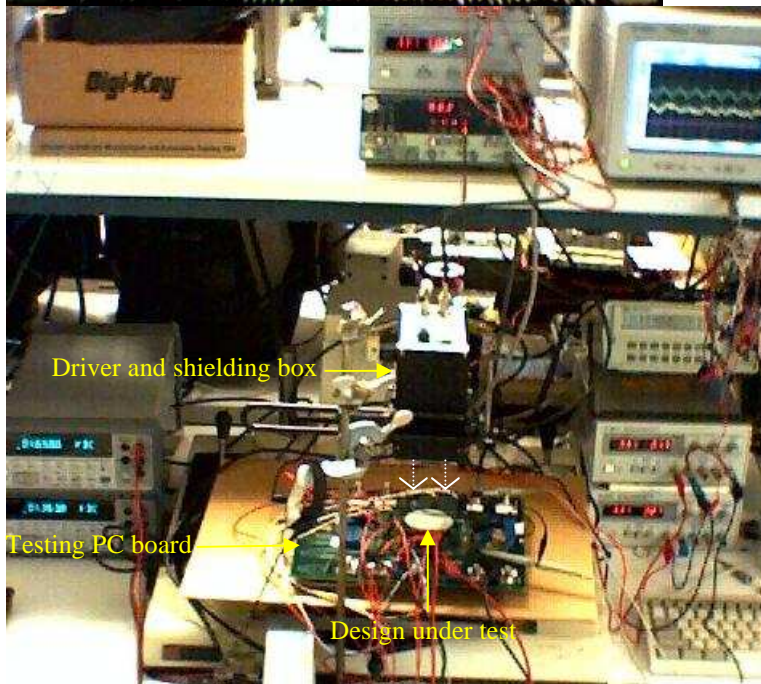Figure 28. Die photo of a prototype chip. (Fabricated in April 2004 via TSMC 0.35 um technology)



Figure 29. Testing bench

A. Photodiode

On-chip N-well/P-substrate photodiode was implemented for each pixel with the N-well size of about 25 um x 10 um, as shown in Fig. 30. A single independent photodiode was also placed in a spare area of the chip for testing purposes, as testing inside the array is not feasible due to layout verification restrictions. The testing shows this independent photodiode generates a dc current from a few nAs to a few hundred nAs, depending on the set-up of the testing bench. The photodiode responses to both single frequency laser and broad-band environment light. Photodiode-in-pixel might have a response different

from this independent one, with the later is usually smaller than the former response. From Fig. 30, the photodiode area is above 10% of the total pixel area.
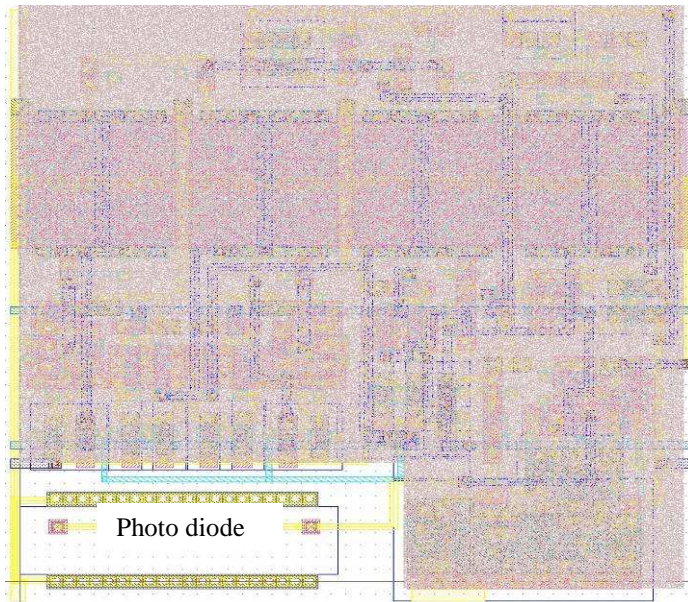


Figure 30. A photodiode in a pixel (labeled as a non-shaded area)

B. Current to voltage conversion and amplification

As shown in previous section, current generated from photodiode can have magnitudes of a range of decades. This current includes large background currents and a relative small signal current. The large background currents usually are either DC or very low frequency current. If a TIA with a frequency response as in Fig. 20 is used, then background currents will also be converted to DC voltage or very low frequency voltage, and the conversion gain is extremely high, which is the same as the signal gain itself. Such a large DC or low frequency voltage basically destroys bias points for the small signal, as well as overwrites the small signal voltage. This challenge, generally called dynamic range, is one of the two key challenges to the whole design.

Typically, two methods could be used for a wide dynamic range. One is dc current canceling, and the other is to design the TIA to have a band-pass frequency response feature. The latter one was used in this design, with its schematic shown in Fig. 31 and frequency response shown in Fig. 32.
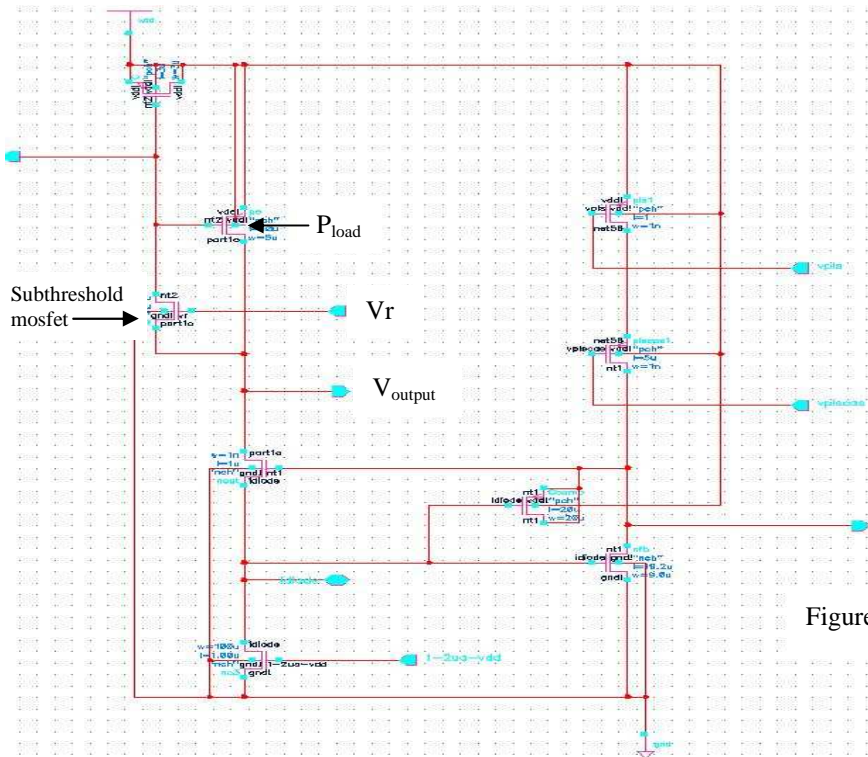
Figure 31. Schematic of on-chip improved TIA

This improved TIA, based on Fig. 17, has an extra subthreshold MOSFET to form a feedback loop with $P_{load}$. Thus, the output load is roughly same for a small signal current, but is much low for a DC or very low frequency current. The output voltage will therefore be a small signal voltage around DC bias points that still keep TIA in the linear transimpedance region, no matter what the background light would be. The external voltage (labeled as "Vr") at the gate of subthreshold MOSFET could be used to adjust the frequency response. Fig. 33 shows the parametric AC responses of TIA under different background currents. Fig. 34 shows the parametric transient response of TIA under different background currents. The background currents vary from 50 nAs to 450 nAs, while the signal current is kept at 5 nAs peak-to-peak.

Although simulation results were quite good even after we intentionally added a large offset to mimic imperfect variations in real chip, the chip testing revealed several modeling issues due to the problems of either foundry-supplied models or the simulator. In Fig. 35, a voltage output of TIA in the testing pixel was obtained only when the light intensity and "Vr" were very carefully adjusted. The "Vr" value in this case is 1 V, which is quite different from the value 0.3 V used in simulation. However, this output was not stable on the oscilloscope. Two further testing were conducted:

1). To mimic the offset of bias at different pixels on the chip, a little deviation of "Vr" from 1 V, like a few millivolts, was introduced. The output DC voltage was observed up or down more than a few hundred millivolts, while the amplitude of output ac signal voltage reduced significantly. More deviations then totally drove output to near supply rails, with almost no signal ac voltage. The correct result should be no significant effect because normal offsets are already taken into consideration of the design.

2). If we kept "Vr" at the same and moved the testing pixel about a few hundreds micron, same effects were observed. This test mimics the pixels at different positions on the chip under the same light intensity. Due to same illumination, the correct result should be that every pixel has the same output, both dc level and ac magnitude, no matter where the pixel is located.
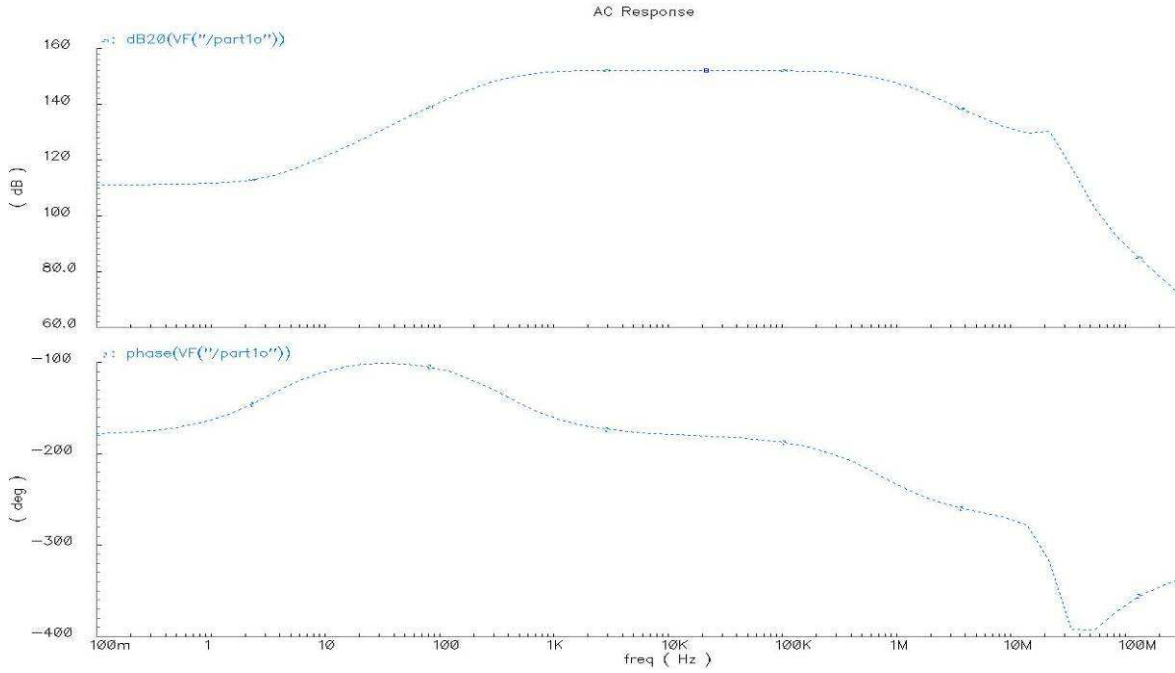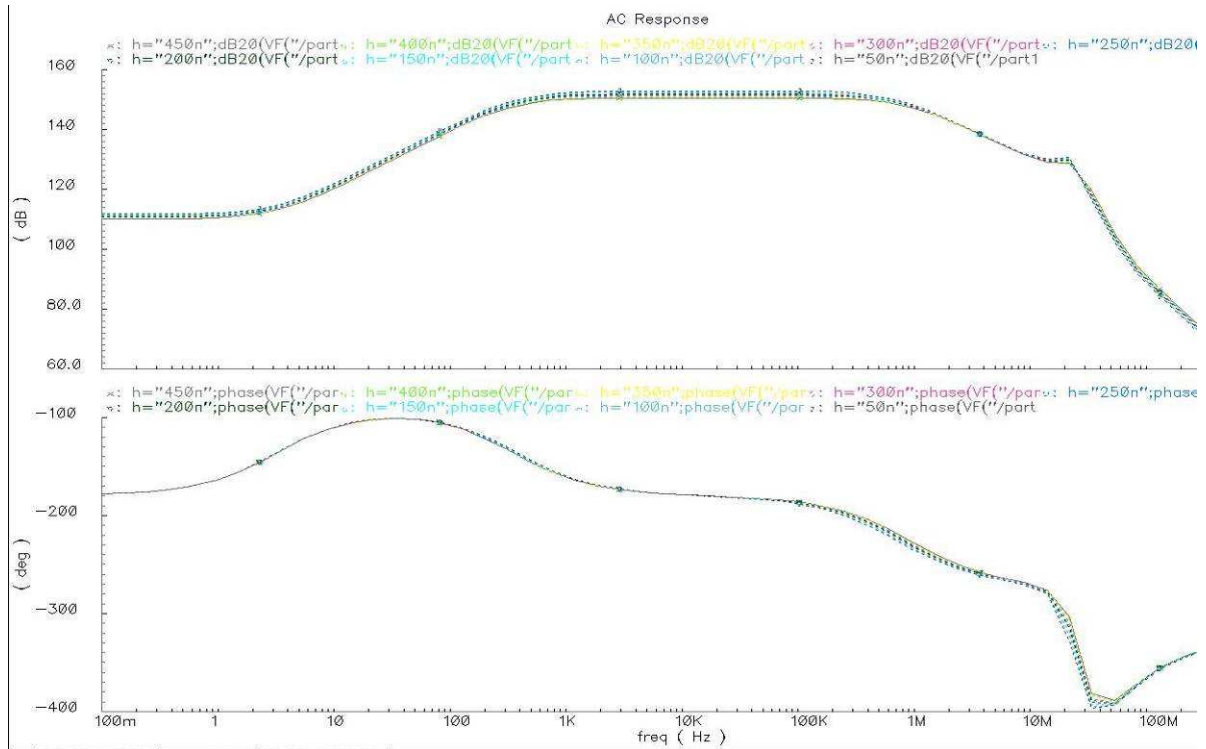


Figure 32. AC response of TIA

Figure 33. Parametric AC responses of TIA under different background currents (the responses are the same no matter the background currents)
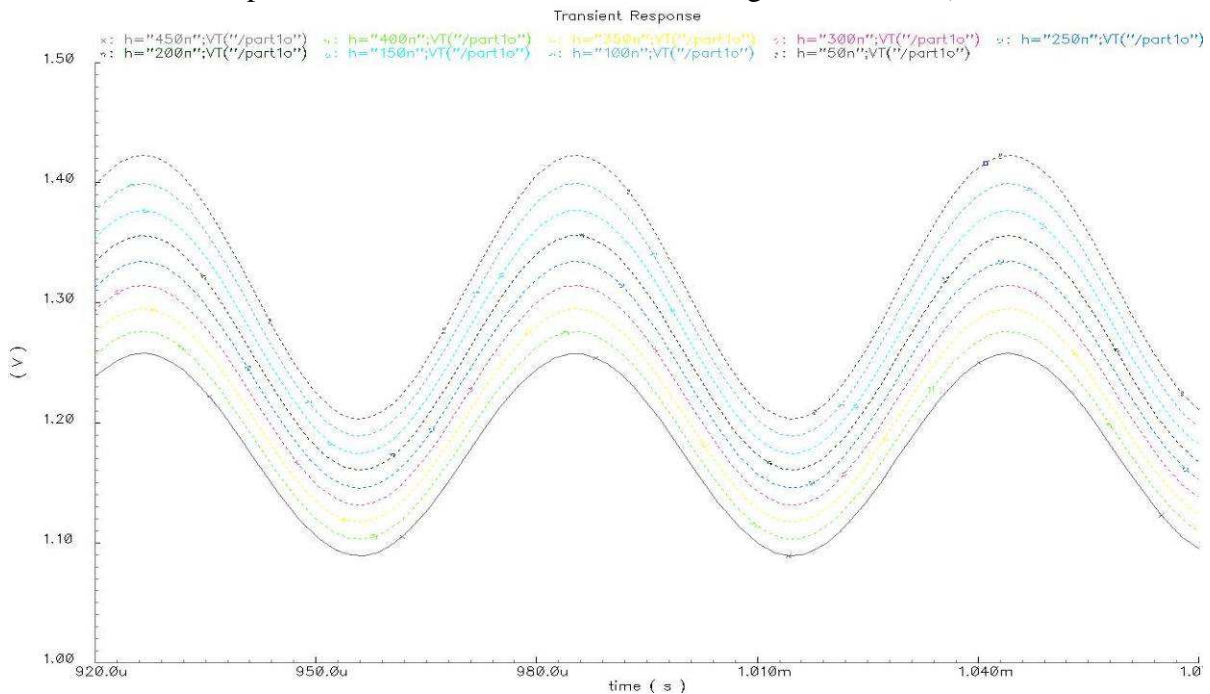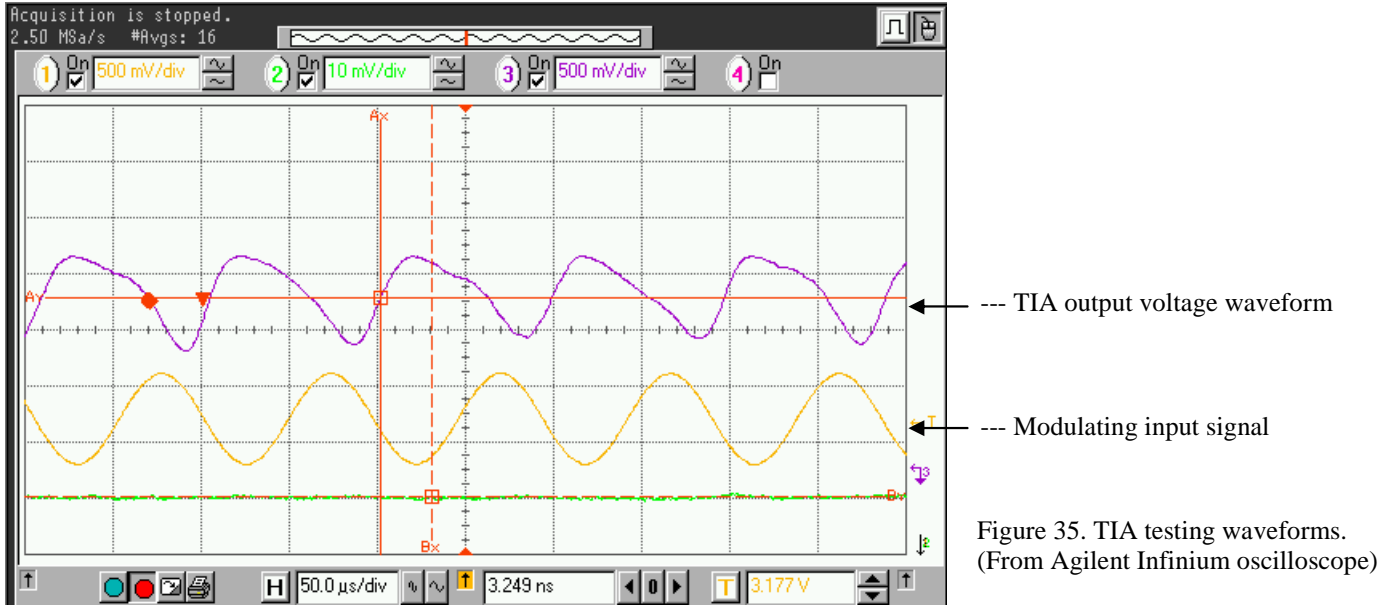


Figure 34. Parametric transient response of TIA under different background currents ( AC outputs are same due to same input signal current. DC levels can be adjusted to a single value in a subsequent stage )

Acquisition is stopped.
2.50 MSa/s   #Avgs: 16

--- TIA output voltage waveform

--- Modulating input signal

Figure 35. TIA testing waveforms.
(From Agilent Infinium oscilloscope)

To find out the reasons, the nodes' voltages were measure throughout the TIA testing pixel. Most nodes' voltages were close to simulation values, except those around the subthreshold MOSFET, which also includes output node. Interestingly, if "Vr" is adjusted to let this MOSFET in the triode region, then all nodes will be very close to simulation values. Therefore, the MOSFET under subthreshold has simulation results different from real chip testing, due to either device model inaccuracy or simulator problem, both could be made worse if a feedback loop exists around this subthreshold device, just as in our design. Our testing shows the transition in subthreshold region is very sharp, so that a stable operation point is very difficult to find and is prone to various tiny offsets, i.e. too sensitive for array operation, which inherently has various offsets. But in simulations, even with a large offset, the device has a wide range for stable operation points.

C. Frequency selective filtering

Filtering at very low corner frequencies, with all on-chip components and small area requirement, is another key challenge in the whole design. Our frequency selective filtering was tested individually, and the results were roughly as simulations. With a comparison with Fig. 22,  Fig. 36 shows that both cases are as expected.
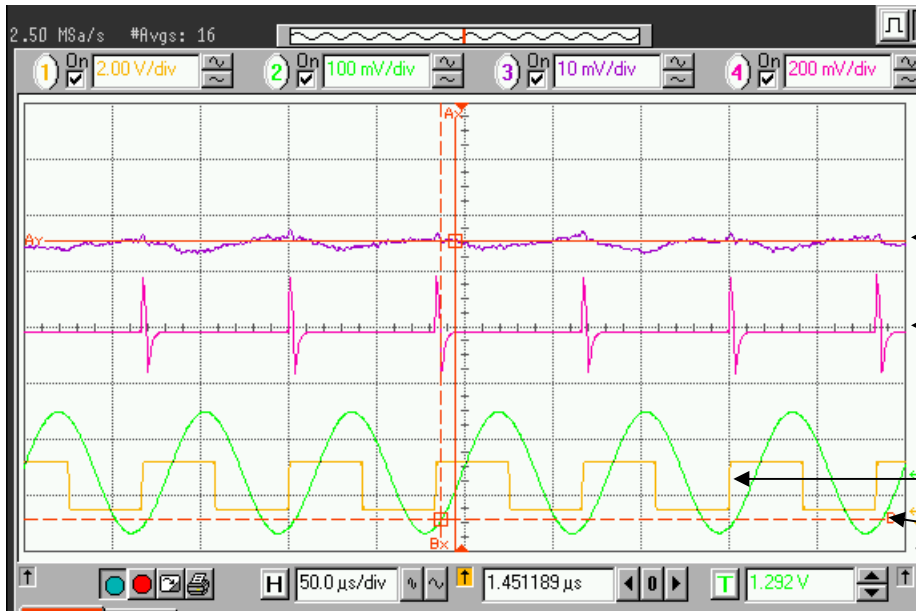
**Same frequency**

--- Final voltage after low pass filter of removing spikes

--- A flat voltage at sampling-hold capacitor (sampled at rising edge of yellow waveform, which is the clock signal)

--- sampling point

--- input signal
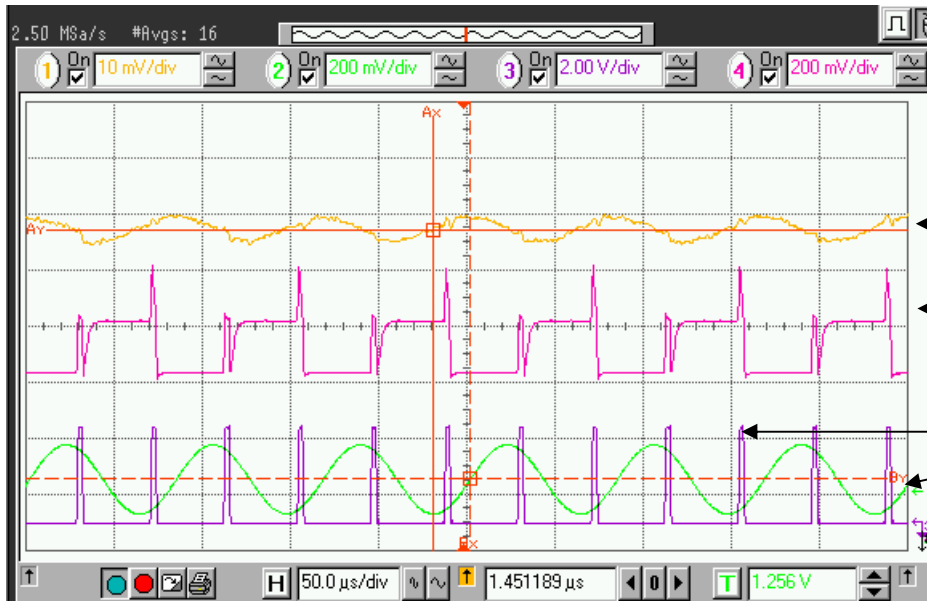


**Different frequencies**

--- Final voltage after low pass filter of averaging and removing spikes

--- Step-wise voltage waveform at sampling-hold capacitor ( sampled at twice of the  signal frequency )

--- sampling point
--- input signal

Figure 36. Frequency selective filter
testing waveforms
(From Agilent Infinium oscilloscope)

Our frequency selective filter has the advantages of adjustable very low corner frequency with very small area and power consumption, with all components fitting in the 50 um X 50 um pixel, as shown in Fig. 37. The low pass filter included could reach a corner frequency of 1 KHz, as shown in Fig. 38.
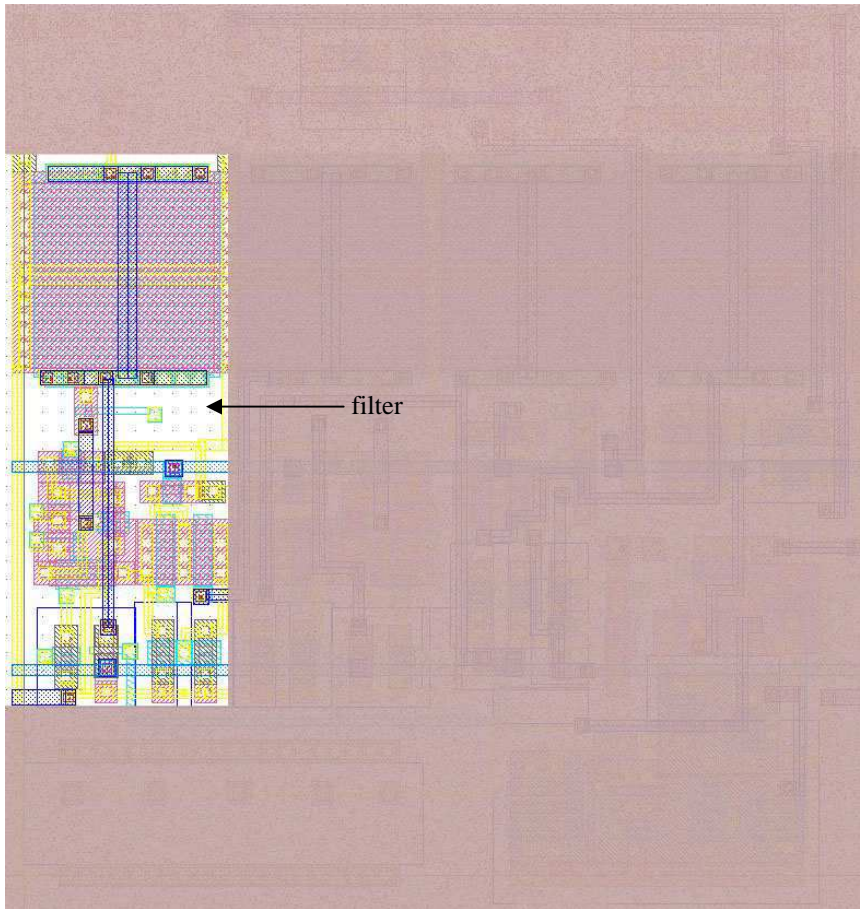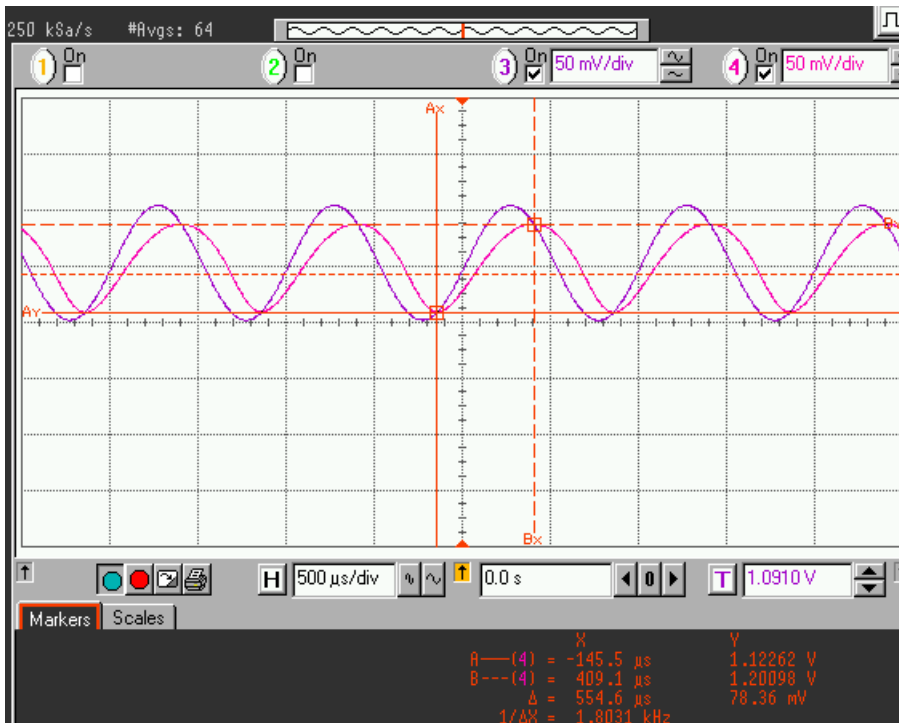
Figure 37. Filter layout in the pixel



Figure 38. On-chip low pass filter with adjustable corner frequency at around 1 KHz

## D. Shift register

The shift register was designed to shift, one by one, the results of 34 x 34 pixels off the chip. It is implemented in static logic circuits for array testing purposes, and verified to be correct on chip. The schematic of the shift register is shown in Fig. 39. This shift register can fulfill the requirement of the array operation speed, i.e. 20 frames per second.
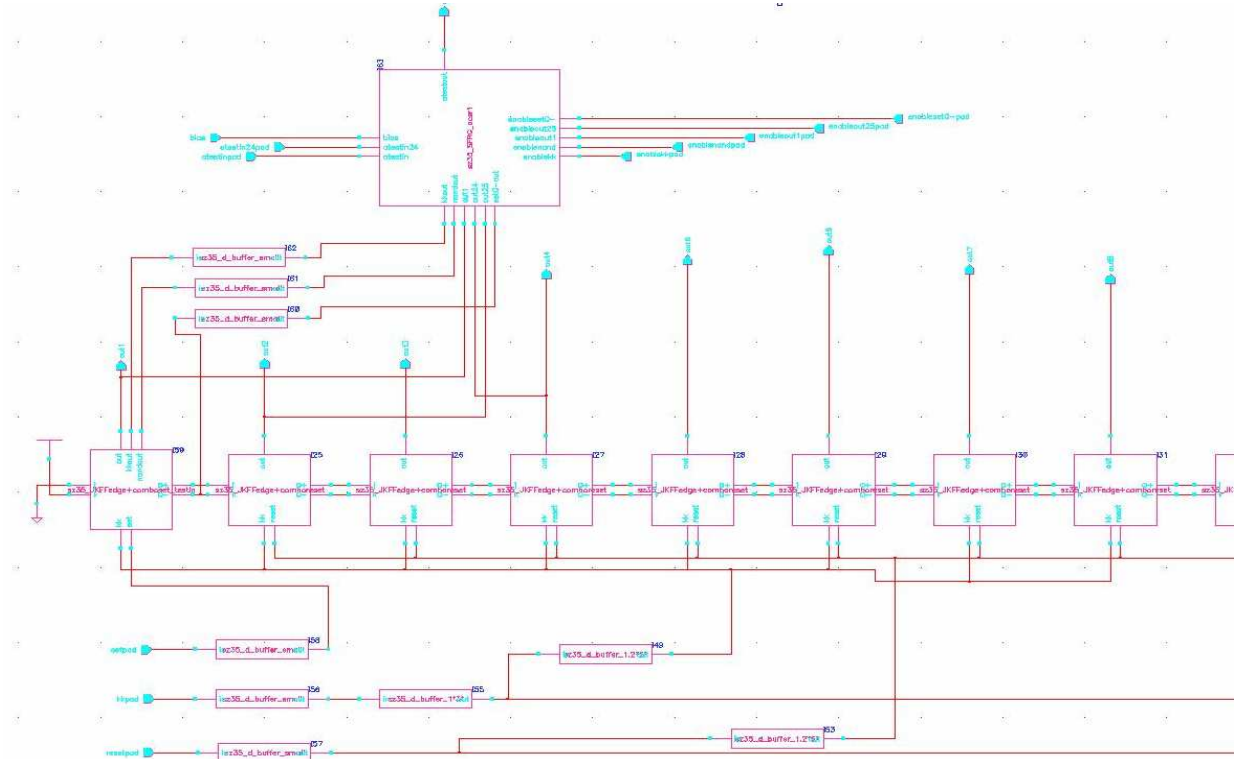


Figure 39. Shift register schematic

## E. Testing bench design

A testing bench was set up for testing photodiodes, shift registers, testing pixels and the array. A 4-layer PC board was designed and fabricated for testing chip with BGA fixtures. In addition, several driving circuits for modulating laser diode and LEDs were designed and implemented on separate perf boards. For shielding and anti-interference purpose, the driver circuit board was enclosed in a specially designed metal case with one side covered by shielding/conductive glass. Power supplies (some with very large current rating), digital multimeters, programmable function generators and digital oscilloscopes were used in testing. Significant coupling problems arise from high speed clocks and fast rising edges, and thus cause spurious signals on the testing pins. This could be more

serious for the array testing once the TIA problem solved. Therefore, a special design project for a high speed testing board is necessary for any future progress.


## V. Conclusions and Suggestions

We have designed, fabricated and tested a photo-detection chip. The photo-detecting fill factor is above 10 % in a pixel of area of 50 um X 50 um, with the chip has an array of 34 x 34 pixels. Our testing in Fig. 22 shows that, if the TIA background light sensitivity problem is solved, the design has a good signal-to-noise ratio. Power consumption simulated for each pixel is less than 1 mW.  Frame rate from simulation is  20 frames/second.

We identified the key problems in the design, and solved one of the challenges. The solution to the other problem, i.e. adaptive background light, was also investigated. By either obtaining more accurate device models and simulator, or creating innovative circuit techniques, we will be able to solve this problem as well. We are currently working on it and have some workarounds to avoid this problem, and will prototype and test it if future research fund could be provided.

*References*

[1] Mandel, L. and E. Wolf, *Optical Coherence and Quantum Optics*. 1995, New York: Cambridge University Press.
[2] Breckenridge, J.B., *Coherence Interferometer and Astronomical Applications.* Applied Optics, 1972. **11**(12): p. 2996.
[3] Roddier, C. and F. Roddier, *High angular resolution observations of alpha orionis with a rotation shear interferometer.* Astrophysical Journal, Letters to the Editor, 1983. **270**: p. L23.
[4] Roddier, C. and F. Roddier, *An image reconstruction of Alpha Orionis.* Astrophysical Journal, Letters to the Editor, 1985. **295**: p. L21.
[5] Chelli, A. and J.-M. Mariotti, *Visibility and phase analysis for image and pupil plane interferometry at optical wavelengths.* Astronomy and Astrophysics, 1986. **157**: p. 372.
[6] Roddier, C. and F. Roddier, *Interferogram analysis using Fourier transform techniques.* Applied Optics, 1987. **26**: p. 1668.
[7] Roddier, F., *Interferometric imaging in optical astronomy.* Physics Report, 1988. **170**: p. 97.
[8] Mariotti, J.-M. and e. al., *Pupil plane interferometry in the near infrared.* Astronomy and Astrophysics, 1992. **255**: p. 462.
[9] B. Razavi, *Design of Analog CMOS integrated circuits*. McGraw-Hill, 2000.
[10] R. Narayan, Master thesis, ECE, University of Virginia, May, 2003
[11] A. Gupta, Master thesis, ECE, University of Virginia, May, 2003
[12] S. Sze, *Physics of Semiconductor Devices*, Chapter. 13, John Wiley & Sons, 1981

[13] S. Zhou, Project paper, Department of Electrical and Computer Engineering, UVA, Dec. 2004